Available online at www.sciencedirect.com
SCIENCE DIRECT®
Comput. Methods Appl. Mech. Engrg. 193 (2004) 5195–5222
Computer methods in applied mechanics and engineering
www.elsevier.com/locate/cma

Computational strategies for predictive geology with reference to salt tectonics

D. Perić [a,*], A.J.L. Crook [b]

[a] Department of Civil Engineering, University of Wales Swansea, Singleton Park, Swansea SA2 8PP, UK
[b] Rockfield Software Ltd. Technium, King's Road, Prince of Wales Dock, Swansea SA1 8PH, UK

Received 24 October 2003; received in revised form 23 January 2004; accepted 23 January 2004

Abstract

This work is concerned with aspects of computational strategies for predictive geology with particular reference to the field of salt tectonics. The computational approach is based on the Lagrangian methodology incorporating: (i) large deformations of inelastic solids at finite strains, (ii) constitutive models for generic inelastic materials suitable for description of simultaneously active elasto-plastic, viscoplastic and viscoelastic behaviour, (iii) an adaptive strategy for modelling of large deformations of inelastic solids at finite strains. Apart from its economic importance, salt tectonics, and in particular formation of salt diapirs, is considered to be representative for many geological processes in the Earth's crust. A number of numerical simulations are provided to illustrate the scope and benefits of the developed computational approach. These include the formation of the salt diapirs due to (i) compression and folding, (ii) thin skinned extension, and (iii) simulation of salt diapirism due to progradation on a basin scale.

Keywords: Predictive geology; Salt tectonics; Nonlinear finite element analysis; Large inelastic strains; Lagrangian methodology; Adaptive strategies; Diapir formation

1. Introduction

1.1. Remarks on modelling of salt tectonics

Salt tectonics has been a focus of intensive research for some time [24,25,6,38,49,54]. Salt deformations, and in particular the formation of diapirs, play a major role in the evolution of geological structures in the

* Corresponding author. Tel.: +01792 29 55 42; fax: +01792 29 56 76.
E-mail address: d.peric@swansea.ac.uk (D. Perić).

0045-7825/$ - see front matter
doi:10.1016/j.cma.2004.01.037

Earth's crust, and dominate sediment deformation in a number of different regions including the Gulf of Mexico, the southern North Sea and Niger delta. Salt tectonics has also an important and growing economic relevance. Initially interest in salt tectonics came from the petroleum industry, since oil and gas traps are often associated with salt domes [38]. Recently, the motivation also comes from nuclear industry, with particular interest related to the storage of radioactive nuclear waste. This is due to the low permeability of salt and its rheological properties.

It is now widely accepted that the formation of salt diapirs is a consequence of complex interplay between gravity, the rheological properties of the rock materials and the detailed morphology of the area. Although the patterns of salt diapirs are complex, the basic physical phenomenon is gravitationally induced instability, in which light salt rock rises in a denser overburden. This type of instability, in which, in the initially flat surface between two immiscible fluids, the perturbation is introduced at the interface, and as a result the lighter fluid raises above the denser one, is widely encountered in nature and is commonly known as the Rayleigh–Taylor instability (see [11] for physical and theoretical background).

During the last decade or so, the research effort has been focused on establishing the conditions, which apart from the basic Rayleigh–Taylor instability, may influence and promote the formation of salt diapirs. This included a large number of experimental studies based on physical (analog) modelling [6,38,50,51,19,18], and mathematical modelling of simple and carefully designed qualitative model problems [52]. Due to difficulties in establishing the in situ conditions, with obvious implications on uncertainties of the mathematical problem in terms of the boundary and initial conditions, and material properties, a debate has been open, with respect to the conditions that may affect salt deformations. The mostly analog models based studies have revealed a number of different mechanisms influencing salt movement. These include: (i) compression and folding of overburden [17,18,52], (ii) both thick- and thin-skinned extension [17,51,18], (iii) differential loading of overburden including progradation due to sedimentation [50,52], (iv) faulting [51,18], (v) flexural buckling of overburden [48,52], (vi) drag [52], and other mechanisms including sediment accumulation, erosion and dissolution. The additional difficulty is that a number of the above mechanisms can be active simultaneously.

Mathematical modelling has been very useful in establishing qualitative knowledge of the basic mechanisms governing the phenomena associated with salt deformations. The complexity of the physical situation has restricted mathematical studies to analysis of largely simplified model problems that do not reflect details of the morphology encountered in the physical environment. For instance, in the case of simple geometries and material characteristics linear stability theory may provide description of the early stages of the Rayleigh–Taylor instability formation. In the nonlinear range, when amplitude becomes large, analytical solutions exist only for special cases and, in general, one must resort to numerical modelling.

A large number of numerical solutions have been presented for the basic Rayleigh–Taylor instability phenomena, mostly in the context of two immiscible fluid simulations. The numerical approach adopted varies between the authors and a full discussion on their relative merits is beyond the scope of this paper. It may, however, be pointed out that, almost exclusively, numerical modelling relies on the Eulerian approach supplemented with appropriate techniques for fluid interface tracking, such as marker/string or volume-of-fluid techniques [7,41,42]. Such numerical simulations are invariably expensive since high resolutions are required to capture all salient features of the problem. A number of researchers have used a viscous two layer model to study the growth of diapirs [49,54,55]. Often fluids are assumed to follow simple Newtonian constitutive laws, which is at best a very crude approximation of complex rock materials that typically exhibit large deformations at finite strains incorporating viscous, plastic and elastic effects. In addition the standard Eulerian approach does not allow for accurate modelling of faulting which is a common feature in the overburden layers, and is believed to be a cause of the perturbation that promotes the Rayleigh–Taylor instabilities in the salt layer and lead to the formation of salt diapirs. Complex

material models for rock materials and procedures to capture fault development are, however, easily incorporated in the Lagrangian framework.

1.2. Computational approach and scope of the study

Computational strategies based on the finite element method are now well established in many branches of engineering and science, for linear and nonlinear applications. The increasing acceptance of such approaches within both research and industrial environments is due to improved awareness, enhanced maturity of computational models and associated algorithms and, more importantly, dramatic increases in computational power/cost ratios.

Computational modelling of nonlinear solid mechanics problems governed by inelastic material behaviour often requires use of sophisticated constitutive material models formulated in the finite strain regime. Computational modelling of different material phenomena, incorporating elastic, elasto-plastic and viscoelastic material behaviour, has been addressed in many publications during the last two decades or so, and it may be said that, even in the finite strain regime, the computational algorithms for modelling inelastic material behaviour are fairly well established. This is particularly pertinent to the isotropic material response and situations in which different rheological phenomena (elasticity, viscoelasticity, plasticity) can be considered independently from each other. We refer to [2,3,9,10,32,46,57] and references therein for the review of the computational approaches employed in modelling of inelastic materials.

Since constitutive behaviour in geological applications incorporate a large variety of different phenomena, it is appropriate to present a generic methodology for constitutive modelling that may describe inelastic material behaviour, with simultaneous consideration of different constitutive phenomena in the finite strain regime. For this purpose, a generalized constitutive model is described, which is based on combination of the recently introduced computational formulations for modelling of elastic, viscoelastic and elasto-plastic material behaviour at finite strains (see [44,40,35]). The underlying rheological model corresponds to the combined action of an arbitrary number of elastic, elasto-plastic, viscoplastic and possibly viscoelastic rheological components arranged in parallel. Such models, termed often as the overlay or fraction models, have previously been used in constitutive description of complex material behaviour mostly in the area of geomechanics. Extensive discussion of such constitutive models, including physical motivation and thermodynamic basis, have been provided in [4]. In the present work attention is restricted to situations, in which the behaviour of each rheological component is isotropic. For alternative formulations of generalized material models incorporating superimposed constitutive models and further references we refer to [23,15].

In the past both Eulerian and Lagrangian formulations have been used in modelling the large deformation of geological structures. The standard Eulerian formulation is normally based on a fixed grid covering the problem domain. For some problems, however, localised mesh refinement may be necessary. The critical aspect of the Eulerian approach is modelling the free surfaces and interfaces. Among a number of different interface tracking techniques the most widely used are [42]: (i) marker/string methods, (ii) volume-of-fluid techniques, and (iii) more recent techniques based on the level set method [41]. Although some important advances have recently been achieved in modelling flows with free surfaces and interfaces [7,41], the interface tracking techniques suffer from the loss of accuracy along the interface, which may lead to inadequate resolution of the interface physics for certain classes of problems. In addition, the Eulerian formulation does not provide a natural setting for modelling of complex material behaviour of both the continua and interfaces.

The main advantages of the Lagrangian methodology, which is based on the reference configuration that moves with particles [1,37], are: (i) intrinsic modelling of the free surfaces and interfaces between different phases of the system, (ii) direct modelling of material properties, which is important for

complex material behaviour. The main disadvantage of the Lagrangian approach is that it suffers from excessive mesh distortion due to often very large particle displacements, necessitating frequent remeshing during the simulation. Apart from the additional expense, remeshing may also degrade the accuracy of the computation due to frequent mapping of the relevant variables between different meshes.

The so-called Arbitrary Lagrangian–Eulerian (ALE) method is also often employed for flow problems with free surfaces and interfaces. However, depending on the formulation, the ALE inherits features of both Eulerian and Lagrangian methodologies. For instance, for large deformations problems the ALE reduces but does not completely remove the need for remeshings.

The computational approach described in this work is based on the Lagrangian method, which is complemented by robust and efficient adaptive meshing techniques. Such methodology has already been successfully employed in computational modelling of inelastic solids [32,33]. The Lagrangian formulation allows accurate tracking of the free surface, and provides a natural framework for computational modelling of complex interface phenomena, which may also incorporate frictional contact phenomena. It is argued in this work that the Lagrangian computational approach offers a natural framework for simulation of the salt diapir formation and similar important geological processes.

The outline of the paper is as follows: Sections 2 and 3 give a brief review of the basics of continuum mechanics and constitutive description at finite strains. Some aspects of numerical integration at the local and global level are provided in Sections 4 and 5, respectively. Section 6 reviews aspects of adaptive strategies for large deformations of inelastic materials. A number of numerical simulations are provided in Section 7 to illustrate the scope and benefits of the developed computational approach. These include examples of the diapir formation under both thin skinned compression and extension, together with a large scale simulation of salt diapirism due to progradation.

2. Preliminaries

2.1. Geometry and kinematics

Consider a generic continuum body $\mathscr{B}$ which occupies a region of the three-dimensional Euclidean space $\mathbb{R}^3$ in its reference configuration, with boundary $\partial\mathscr{B}$. Let $\mathscr{B}$ be subjected to a motion $\boldsymbol{\varphi}$ so that for each time t, the deformation $\boldsymbol{\varphi}(\cdot, t) : \mathscr{B} \to \mathbb{R}^3$ maps each material particle $\boldsymbol{X}$ of $\mathscr{B}$ into the position $\boldsymbol{x}$ it occupies at time t. The set $\boldsymbol{x} = \boldsymbol{\varphi}(\boldsymbol{X}, t)$ is called the current or deformed configuration.

The two point tensor $\boldsymbol{F}$ defined by $\boldsymbol{F}(\boldsymbol{X}, t) = \mathrm{D}\boldsymbol{\varphi}(\boldsymbol{X}, t) = \frac{\partial \varphi_i}{\partial X_I} \boldsymbol{e}_i \otimes \boldsymbol{E}_I$ is termed the deformation gradient, where $\{\boldsymbol{E}_I\}_{I=1,2,3}$ and $\{\boldsymbol{e}_i\}_{i=1,2,3}$ are fixed orthonormal bases in the reference and deformed configuration, respectively, typically chosen to be coincident with the standard basis in $\mathbb{R}^3$. The Jacobian of the mapping can be represented as $J = \det \boldsymbol{F}$.

2.2. Momentum balance

Denote by $\boldsymbol{\sigma}(\boldsymbol{x}, t)$ the standard Cauchy stress tensor $\boldsymbol{\sigma}(\boldsymbol{x}, t)$ such that $\boldsymbol{t}(\boldsymbol{x}, t, \boldsymbol{n}) = \boldsymbol{\sigma}\boldsymbol{n}$, where $\boldsymbol{t}(\boldsymbol{x},t,\boldsymbol{n})$ is the traction vector and $\boldsymbol{n}$ is the normal. The local form of the (linear) momentum balance can then be expressed as

$$\nabla \cdot \boldsymbol{\sigma} + \rho \boldsymbol{b} = \rho \boldsymbol{a}, \tag{1}$$

where $\boldsymbol{b}$ is the body force density, and $\boldsymbol{a} = \dot{\boldsymbol{u}}$ stands for the acceleration field and $\boldsymbol{u}$ is the velocity.

The continuity of forces on the portion $\Gamma_h \subset \partial\mathscr{B}$ of the boundary $\partial\mathscr{B}$ implies the standard boundary condition

$$\boldsymbol{\sigma n} = \bar{\boldsymbol{t}} \quad \text{on } \Gamma_h \times \mathbb{I}, \tag{2}$$

where $\mathbb{I} = [0, T] \subset \mathbb{R}^+$ is the time interval of interest.

2.3. Nonlinear kinematics and geometry description

The chief hypothesis underlying the present approach to the modelling of large deformations of inelastic solids at finite strains is the *multiplicative split* of the deformation gradient into elastic and inelastic parts:

$$\boldsymbol{F} = \boldsymbol{F}^e \boldsymbol{F}^i. \tag{3}$$

This assumption admits the existence of a local unstressed intermediate configuration. Due to its suitability for the computational treatment of finite strain elasto-plasticity, the hypothesis of the multiplicative decomposition has been widely employed in the computational mechanics literature in modelling both elasto-plastic [14,44,13,28] and viscoelastic solids [43,40] (see also [23] for an alternative point of view).

Following the multiplicative split of $\boldsymbol{F}$, the velocity gradient, $\boldsymbol{l} := \dot{\boldsymbol{F}}\boldsymbol{F}^{-1}$, can be decomposed additively as

$$\boldsymbol{l} = \boldsymbol{l}^e + \boldsymbol{l}^i, \qquad \text{with } \boldsymbol{l}^e := \dot{\boldsymbol{F}}^e \boldsymbol{F}^{e-1} \quad \text{and} \quad \boldsymbol{l}^i := \boldsymbol{F}^e \dot{\boldsymbol{F}}^i \boldsymbol{F}^{i^{-1}} \boldsymbol{F}^{e-1}. \tag{4}$$

Similarly, the stretching tensor, $\boldsymbol{d} := \mathrm{sym}[\boldsymbol{l}]$, can be decomposed as

$$\boldsymbol{d} = \boldsymbol{d}^e + \boldsymbol{d}^i, \qquad \text{with } \boldsymbol{d}^e := \mathrm{sym}[\boldsymbol{l}^e] \quad \text{and} \quad \boldsymbol{d}^i := \mathrm{sym}[\boldsymbol{l}^i]. \tag{5}$$

In what follows it is convenient to introduce the left Cauchy–Green tensor $\boldsymbol{b}^e := \boldsymbol{F}^e \boldsymbol{F}^{eT} = \boldsymbol{F}(\boldsymbol{F}^i)^{-1}(\boldsymbol{F}^i)^{-T}\boldsymbol{F}^T$. In order to provide a concise and unified constitutive modelling framework for the formulation of the evolution laws it has proved convenient to make use of the so-called *Lie derivative* of the left Cauchy–Green tensor (see [46] for the physical motivation and further details)

$$\mathscr{L}_v \boldsymbol{b}^e := \boldsymbol{F}\{\partial_t[\boldsymbol{F}^{-1}\boldsymbol{b}^e\boldsymbol{F}^{-T}]\}\boldsymbol{F}^T = \dot{\boldsymbol{b}}^e - \boldsymbol{l}\boldsymbol{b}^e - \boldsymbol{b}^e\boldsymbol{l}^T. \tag{6}$$

2.4. Thermodynamic basis

Let $\psi(\boldsymbol{b}^e, \boldsymbol{\xi})$ be the free energy and denote by $\boldsymbol{\xi}$ the set $\boldsymbol{\xi} = \{\xi_1, \xi_2, \ldots, \xi_k\}$ of internal variables associated with dissipative mechanisms. The time derivative of the free energy then reads

$$\dot{\psi}(\boldsymbol{b}^e, \boldsymbol{\xi}) = \frac{\partial\psi}{\partial\boldsymbol{b}^e} : \dot{\boldsymbol{b}}^e + \frac{\partial\psi}{\partial\boldsymbol{\xi}} \cdot \dot{\boldsymbol{\xi}}. \tag{7}$$

By introducing the definition (6) and by taking into account the elastic isotropy, the rate of change of free energy can be expressed as

$$\dot{\psi} = \left(2\frac{\partial\psi}{\partial\boldsymbol{b}^e}\boldsymbol{b}^e\right) : \left(\boldsymbol{d} + \frac{1}{2}(\mathscr{L}_v\boldsymbol{b}^e)\boldsymbol{b}^{e-1}\right) + \frac{\partial\psi}{\partial\boldsymbol{\xi}} \cdot \dot{\boldsymbol{\xi}}. \tag{8}$$

By standard arguments, from the *Clausius–Duhem* inequality

$$\boldsymbol{\tau} : \boldsymbol{d} - \dot{\psi} \geqslant 0, \tag{9}$$

the constitutive equation for the Kirchhoff stress is obtained as

$$\boldsymbol{\tau} = 2\frac{\partial \psi}{\partial \boldsymbol{b}^e}\boldsymbol{b}^e, \tag{10}$$

and the non-negative dissipation requirement is reduced to

$$\boldsymbol{\tau} : \left(-\frac{1}{2}(\mathscr{L}_v \boldsymbol{b}^e)\boldsymbol{b}^{e-1}\right) - \frac{\partial \psi}{\partial \boldsymbol{\xi}} \cdot \dot{\boldsymbol{\xi}} \geqslant 0. \tag{11}$$

3. The constitutive model for large deformations of inelastic solids at finite strains

Some important aspects of constitutive modelling of inelastic solids at finite strains are briefly reviewed in this section. From the outset the attention is restricted to isotropic solids.

3.1. Multiplicative decomposition of the deformation gradient

A useful generalization of the above multiplicative model may be obtained by considering the multiplicative decomposition of the deformation gradient $\boldsymbol{F}$ in terms of $k = 1, 2, \ldots, n_{\text{rheol}}$ rheological components arranged in parallel as shown in Fig. 1. The relationships

$$\boldsymbol{F} = \boldsymbol{F}_1^e \boldsymbol{F}_1^i = \boldsymbol{F}_2^e \boldsymbol{F}_2^i = \boldsymbol{F}_3^e \boldsymbol{F}_3^i = \cdots \tag{12}$$

then represent generalization of the multiplicative split of a single rheological component. The free energy of a material model, can then be represented as the sum of the free energies of the rheological components, i.e.

$$\psi = \psi_1(\boldsymbol{b}_1^e, \boldsymbol{\xi}_1) + \psi_2(\boldsymbol{b}_2^e, \boldsymbol{\xi}_2) + \psi_3(\boldsymbol{b}_3^e, \boldsymbol{\xi}_3) + \cdots \tag{13}$$

By considering the Clausius–Duhem inequality (9), as suggested in Section 2.4, and by employing the elastic isotropy and the properties of the inner product, the following relationship can be obtained

$$\left(\boldsymbol{\tau} - \sum_k 2\frac{\partial \psi_k}{\partial \boldsymbol{b}_k^e}\boldsymbol{b}_k^e\right) : \boldsymbol{d} + \sum_k 2\frac{\partial \psi_k}{\partial \boldsymbol{b}_k^e}\boldsymbol{b}_k^e : \left(-\frac{1}{2}(\mathscr{L}_v \boldsymbol{b}_k^e)\boldsymbol{b}_k^{e-1}\right) - \sum_k \frac{\partial \psi_k}{\partial \boldsymbol{\xi}_k} \cdot \dot{\boldsymbol{\xi}}_k \geqslant 0. \tag{14}$$

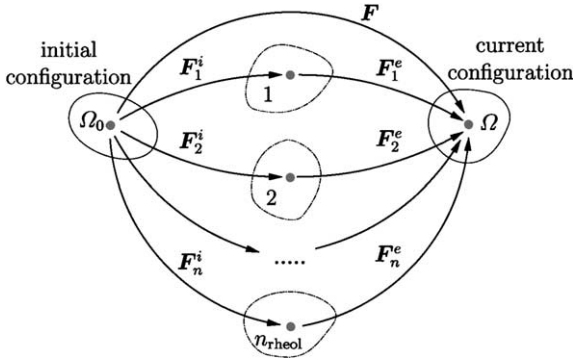

Fig. 1. Parallel split of the deformation gradient.

The standard argument then yields the relation

$$\boldsymbol{\tau} = \sum_k \boldsymbol{\tau}_k \qquad \text{where } \boldsymbol{\tau}_k := 2\frac{\partial \psi_k}{\partial \boldsymbol{b}_k^e}\boldsymbol{b}_k^e, \quad k = 1, 2, \ldots, n_{\text{rheol}}. \tag{15}$$

In order for the inequality (14) to be satisfied, each rheological component must satisfy the non-negative dissipation requirement, that is,

$$\boldsymbol{\tau}_k : \left(-\frac{1}{2}(\mathscr{L}_v \boldsymbol{b}_k^e)\boldsymbol{b}_k^{e-1}\right) - \frac{\partial \psi_k}{\partial \boldsymbol{\xi}_k} \cdot \dot{\boldsymbol{\xi}}_k \geqslant 0, \quad k = 1, 2, \ldots, n_{\text{rheol}}. \tag{16}$$

3.2. Finite strain elasto-viscoplasticity and elasto-plasticity

By starting from the thermodynamic framework briefly described in Section 2.4 it is possible to develop constitutive equations for elasto-plastic and elasto-viscoplastic solids at finite strains. Without going into details of what can already be viewed as the standard approach (see [44,45,29,32,46,34,3] for details), the constitutive equations for a single split of the deformation gradient $\boldsymbol{F} = \boldsymbol{F}^e\boldsymbol{F}^p$ in elastic and inelastic parts may be expressed as follows:

- elasto-viscoplasticity:

$$\boldsymbol{\tau} = 2\frac{\partial \psi}{\partial \boldsymbol{b}^e}\boldsymbol{b}^e, \quad q = -\frac{\partial \psi}{\partial \xi}, \tag{17}$$

$$-\frac{1}{2}(\mathscr{L}_v \boldsymbol{b}^e)\boldsymbol{b}^{e-1} = \frac{\langle \phi \rangle}{\eta}\frac{\partial \phi}{\partial \boldsymbol{\tau}}, \quad \dot{\xi} = \frac{\langle \phi \rangle}{\eta}\frac{\partial \phi}{\partial q}, \tag{18}$$

- elasto-plasticity:

$$\boldsymbol{\tau} = 2\frac{\partial \psi}{\partial \boldsymbol{b}^e}\boldsymbol{b}^e, \quad q = -\frac{\partial \psi}{\partial \xi}, \tag{19}$$

$$-\frac{1}{2}(\mathscr{L}_v \boldsymbol{b}^e)\boldsymbol{b}^{e-1} = \dot{\gamma}\frac{\partial \phi}{\partial \boldsymbol{\tau}}, \quad \dot{\xi} = \dot{\gamma}\frac{\partial \phi}{\partial q}, \tag{20}$$

$$\phi \leqslant 0, \quad \dot{\gamma} \geqslant 0, \quad \phi\dot{\gamma} = 0. \tag{21}$$

Here $\phi = \widetilde{\phi}(\boldsymbol{\tau}, q)$ represents the yield function, q is the stress conjugate to the internal variable ξ, $\langle \cdot \rangle$ is the ramp function and γ is the consistency parameter. We point out that the flow rule in the form $(20)_1$ (or equivalently $(18)_1$), was first proposed by Simo and Miehe [45].

3.2.1. Viscoplastic model: power law viscoplastic potential

The material model for elasto-viscoplasticity considered in this work is based on the von Mises yield criterion and the power law type of the viscoplastic potential [36,29,12]. The set of constitutive equations describing the model is given as

$$\phi(\boldsymbol{\tau}, \tau_0) = F(\boldsymbol{\tau}) - \tau_0, \tag{22}$$

$$F(\boldsymbol{\tau}) = \sqrt{3J_2}, \tag{23}$$

$$-\frac{1}{2}(\mathscr{L}_v \boldsymbol{b}^e)\boldsymbol{b}^{e-1} = \gamma_\circ \langle \Psi \rangle \frac{\partial \phi(\boldsymbol{\tau})}{\partial \boldsymbol{\tau}}, \tag{24}$$

where $J_2(\boldsymbol{\tau})$ is the second invariant of the deviatoric stress, τ_0 is the yield stress and γ_0 is the fluidity. Furthermore, the viscoplastic flow potential is introduced as

$$\Psi(\boldsymbol{\tau}) = \left(\frac{F(\boldsymbol{\tau})}{\tau_\circ}\right)^N - 1, \tag{25}$$

where N is the material parameter representing the rate-sensitivity of the material. The evolution problem described by (22)–(25) is widely accepted as a description of the rate-dependent deformations of solids and has a firm experimental basis [36,29]. A detailed mathematical and experimental study of this model is provided in [29]. In this work it will be used as a constitutive model of salt behaviour, and, in some instances for description of overburden.

3.2.2. Elasto-plastic model: Mohr–Coulomb yield criterion

The Mohr–Coulomb yield function, written in terms of the principal stresses $\tau_1 > \tau_2 > \tau_3$, can be expressed as

$$\phi(\boldsymbol{\tau}, c) = (\tau_1 - \tau_3) + (\tau_1 + \tau_3)\sin\theta - 2c\cos\theta, \tag{26}$$

where c denotes the cohesion and θ is the angle of friction. The Mohr–Coulomb yield surface is widely used in description of geomaterials, such as soils, rocks and concrete, whose behaviour is generally characterised by a strong dependence of the yield limit on the hydrostatic pressure [21].

The associated flow rule for the Mohr–Coulomb yield criterion (26) gives the plastic flow as

$$-\tfrac{1}{2}(\mathscr{L}_v \boldsymbol{b}^e)\boldsymbol{b}^{e-1} = \gamma \boldsymbol{N}, \tag{27}$$

$$\boldsymbol{N} \in \partial_{\boldsymbol{\tau}}\phi, \tag{28}$$

thus, in general, identifying the flow direction as a sub-differential of the yield function ϕ with respect to $\boldsymbol{\tau}$.

The plastic flow given by the associated flow rule (27) provides a non-negative volumetric plastic strain rate. This phenomenon, known as the dilatancy, is observed in many geomaterials. However, the dilatancy predicted by the associative Mohr–Coulomb law is often excessive. To overcome this problem, a non-associated flow rule is often used in conjunction with the Mohr–Coulomb yield criterion (26), in which the plastic flow is derived from the flow potential that employs a Mohr–Coulomb yield function with the friction angle θ replaced by a different (usually smaller) angle θ_0. The Mohr–Coulomb yield criterion (27) with non-associative flow rule defined by a friction angle θ_0 will be widely used in this work for constitutive modelling of materials describing overburden. Further details of theoretical and computational modelling of yield criteria containing singularities, such as Tresca and Mohr–Coulomb yield criteria, can be found in [10,34].

3.3. General material models

Inspection of constitutive relations given in Section 3.1 suggests a strategy for designing a generalized material model for large deformations of inelastic solids by combining in parallel arrangement several constitutive components that follow different constitutive laws. The type and number of components to be used in description of a given material will of course depend on the constitutive properties of the material at hand, and will need to be evaluated by a specific material identification procedure.

By considering a combination of a single elastic spring, n_{vp} viscoplastic elements and n_{ep} elasto-plastic elements, the complete set of constitutive equations to be used in description of a generic material is given in Box 3.1.

Box 3.1. Generic material model for inelastic solids

- Stress tensor

$$\boldsymbol{\tau} = \boldsymbol{\tau}_\infty + \sum_k^{n_{\mathrm{vp}}} \boldsymbol{\tau}_k + \sum_k^{n_{\mathrm{ep}}} \boldsymbol{\tau}_k.$$

- Elastic spring

$$\boldsymbol{\tau}_\infty = 2\frac{\partial \psi_\infty}{\partial \boldsymbol{b}}\boldsymbol{b}.$$

- Viscoplastic components ($k = 1, 2, \ldots, n_{\mathrm{vp}}$)

$$\boldsymbol{\tau}_k = 2\frac{\partial \psi_k}{\partial \boldsymbol{b}_k^e}\boldsymbol{b}_k^e, \quad q_k = -\frac{\partial \psi_k}{\partial \xi_k},$$

$$-\frac{1}{2}(\mathscr{L}_v \boldsymbol{b}_k^e)\boldsymbol{b}_k^{e-1} = \frac{\langle \phi_k \rangle}{\eta_k}\frac{\partial \phi_k}{\partial \boldsymbol{\tau}_k}, \quad \dot{\xi}_k = \frac{\langle \phi_k \rangle}{\eta_k}\frac{\partial \phi_k}{\partial q_k}.$$

- Plastic components ($k = 1, 2, \ldots, n_{\mathrm{ep}}$)

$$\boldsymbol{\tau}_k = 2\frac{\partial \psi_k}{\partial \boldsymbol{b}_k^e}\boldsymbol{b}_k^e, \quad q_k = -\frac{\partial \psi_k}{\partial \xi_k},$$

$$-\frac{1}{2}(\mathscr{L}_v \boldsymbol{b}_k^e)\boldsymbol{b}_k^{e-1} = \dot{\gamma}_k\frac{\partial \phi_k}{\partial \boldsymbol{\tau}_k}, \quad \dot{\xi}_k = \dot{\gamma}_k\frac{\partial \phi_k}{\partial q_k},$$

$$\phi_k := \phi(\boldsymbol{\tau}_k, q_k),$$

$$\phi_k \leqslant 0, \quad \dot{\gamma}_k \geqslant 0, \quad \phi_k \dot{\gamma}_k = 0.$$

We refer to [35] for further details the constitutive model, which in addition to combining elastic, viscoplastic and plastic material behaviours at finite strains, also considers viscoelastic material behaviour. The paper also describes the algorithmic treatment and provides some illustrative numerical examples.

4. Numerical integration of the constitutive equations

In the context of a finite element schemes for solution of path dependent problems, given the values of the variables $\{\boldsymbol{\tau}_n, \boldsymbol{b}_n^e, \boldsymbol{\xi}_n\}$ at the beginning of a generic increment $[t_n, t_{n+1}]$, an algorithm for integration of the above constitutive equations is required to obtain the updated values $\{\boldsymbol{\tau}_{n+1}, \boldsymbol{b}_{n+1}^e, \boldsymbol{\xi}_{n+1}\}$ at the end of the increment.

4.1. The exponential map

The crucial point in the derivation of the algorithm adopted in this work is the discretization of the constitutive description for the inelastic evolution laws given in the Box 3.1, by means of a fully implicit exponential approximation [53,14,45,44]. By restricting attention to a single inelastic constitutive component of a generalized material model from the Box 3.1, in the case of the elasto-plastic evolution law, and a

conventional backward Euler approximation, the exponential approximation leads to the following incremental constitutive update of the elastic left Cauchy–Green tensor $\boldsymbol{b}^e$:

$$\boldsymbol{b}^e_{n+1} = \exp(-2\Delta\gamma\partial_\tau\phi)\boldsymbol{b}^{e\,\mathrm{trial}}_{n+1}, \tag{29}$$

where $\boldsymbol{b}^{e\,\mathrm{trial}}_{n+1} := \boldsymbol{f}\boldsymbol{b}^e_n\boldsymbol{f}^T = \boldsymbol{F}\boldsymbol{C}^{i-1}_n\boldsymbol{F}^T$, denotes the so-called trial elastic left Cauchy–Green tensor, and $\boldsymbol{C}^i_n = \boldsymbol{F}^{iT}_n\boldsymbol{F}^i_n$. Similar expressions can be obtained for numerical integration of the evolution laws for finite strain viscoplasticity and viscoelasticity [40,45,35].

4.2. Formulation in the principal directions

It may easily be shown that for the case of isotropic materials the incremental update given by (29) takes place at fixed principal axes fully defined by the trial elastic left Cauchy–Green tensor $\boldsymbol{b}^{e\,\mathrm{trial}}_{n+1}$. This implies that the optimal implementation strategy for solution of a local update (29) is provided by formulation in terms of principal values of the tensors in (29). By performing the spectral decomposition and taking the logarithms of the resulting expressions, the incremental local update of the finite strain elasto-plastic model given in the Box 3.1 can be expressed, in terms of the principal values of the elastic Eulerian logarithmic strain tensor, as

$$\varepsilon^e_{An+1} = \varepsilon^{e\,\mathrm{trial}}_{An+1} - \Delta\gamma\partial_{\tau_A}\phi|_{n+1}, \tag{30}$$

which has the same format of the update formula for the elastic strains of the standard return mapping algorithms of the infinitesimal theory [14,13,28,45,44]. Similar arguments can be applied in formulation of the constitutive updates for other rheological components, including both viscoelastic and viscoplastic constitutive laws.

It should be emphasised that, as a consequence of the exponential mapping in the implicit integration of the inelastic evolution laws, the incompressibility constraint is carried over exactly to the incremental rules (29).

5. The boundary value problem

5.1. Implicit solution procedure

With the principle of virtual work as the basis of kinematically based finite element solution schemes, the corresponding *continuum* incremental boundary value problem is formulated in the spatial configuration as follows: Given an equilibrium state at time t_n, in which $\boldsymbol{\tau}$ and the internal variables of the problem are known, find a configuration defined by the deformation map $\boldsymbol{\varphi}_{n+1}$ at time t_{n+1} such that

$$\int_{\boldsymbol{\varphi}_{n+1}(\Omega)} \left(\frac{1}{J_{n+1}}\boldsymbol{\tau}_{n+1} : \nabla\boldsymbol{\eta} - \rho\boldsymbol{b}_{n+1}\cdot\boldsymbol{\eta}\right)\mathrm{d}v - \int_{\boldsymbol{\varphi}_{n+1}(\partial\Omega_\sigma)} \boldsymbol{t}_{n+1}\cdot\boldsymbol{\eta}\mathrm{d}a = 0 \quad \forall\boldsymbol{\eta}\in\mathscr{V}, \tag{31}$$

where $\boldsymbol{b}_{n+1}$ and $\boldsymbol{t}_{n+1}$ are, respectively, the *body force* and *surface traction* fields referred to the spatial configuration. Note that the symbol ∇ stands for the *spatial gradient* and $\mathscr{V}$ is the *space of virtual displacements*. The Kirchhoff stress $\boldsymbol{\tau}_{n+1}$ in the expression above is delivered as the outcome of the integration algorithm described in Section 4.

The standard Newton–Raphson scheme for solution of the incremental boundary value problem is obtained with the linearization of (31). In this context, assuming that the external forces are configuration-independent, the linearization of the problem reduces to the linearization of the internal virtual work functional, defined by

$$G^{\text{int}}(\boldsymbol{\varphi}_{n+1}, \boldsymbol{\eta}) := \int_{\boldsymbol{\varphi}_{n+1}(\Omega)} \frac{1}{J_{n+1}} \boldsymbol{\tau}_{n+1} : \nabla \boldsymbol{\eta} \, \mathrm{d}v. \tag{32}$$

A standard application of the directional derivative formula to the above functional at a configuration $\boldsymbol{\varphi}_{n+1}^{(i)}$, corresponding to the ith Newton–Raphson iteration, leads to the linearized version

$$DG^{\text{int}}(\boldsymbol{\varphi}_{n+1}^{(i)}, \boldsymbol{\eta}) \cdot \Delta \boldsymbol{d}^{(i)} = \int_{\boldsymbol{\varphi}_{n+1}^{(i)}(\Omega)} \nabla \boldsymbol{\eta} : \mathbf{a}_{n+1}^{(i)} : \nabla (\Delta \boldsymbol{d}^{(i)}) \, \mathrm{d}v, \tag{33}$$

with $\Delta \boldsymbol{d}^{(i)}$ representing the iterative displacement field and $\mathbf{a}_{n+1}^{(i)}$ denoting the *spatial tangent modulus* expressed, in Cartesian components, by

$$\mathsf{a}_{ijkl} = \frac{1}{J} \frac{\partial \tau_{ij}}{\partial F_{kq}} F_{lq} + \sigma_{il} \delta_{jk}, \tag{34}$$

where, for notational convenience, the subscript $n+1$ and superscript i have been omitted.

A straightforward application of the chain rule to (34) leads to the closed form expression:

$$\mathsf{a}_{ijkl} = \frac{1}{2J} [\mathbf{h}^i : \mathbf{n} : \mathbf{b}]_{ijkl} + \sigma_{il} \delta_{jk}, \tag{35}$$

where $\mathbf{h}^i$ is the *consistent tangent material operator* associated with the inelastic stress update, i.e.

$$\mathbf{h}^i := \frac{\partial \boldsymbol{\tau}_{n+1}}{\partial \boldsymbol{\varepsilon}_{n+1}^{e\,\text{trial}}}, \tag{36}$$

with $\boldsymbol{\varepsilon}_{n+1}^{e\,\text{trial}} := \ln[\boldsymbol{b}_{n+1}^{e\,\text{trial}}]$, while the fourth order tensor $\mathbf{n}$ is defined as

$$\mathbf{n} := \frac{\partial \ln[\boldsymbol{b}_{n+1}^{e\,\text{trial}}]}{\partial \boldsymbol{b}_{n+1}^{e\,\text{trial}}} \tag{37}$$

i.e., it is the derivative of the tensor logarithm function at $\boldsymbol{b}_{n+1}^{e\,\text{trial}}$. The closed form expressions for the derivative of the tensor logarithm in 2 and 3-D can be obtained as particular cases of the derivative of a class of isotropic tensor functions derived by Carlson and Hoger [8]. The closed form expression for this derivative is particularly simple in 2-D and was provided by de Souza Neto and Perić [47,34] (for a similar approach see also [22]). Finally, the Cartesian components of $\mathbf{b}$ are defined by

$$\mathsf{b}_{ijkl} := \delta_{ik} (\boldsymbol{b}_{n+1}^{e\,\text{trial}})_{jl} + \delta_{jk} (\boldsymbol{b}_{n+1}^{e\,\text{trial}})_{il}. \tag{38}$$

Note that $\mathbf{h}^i$ is the only material related contribution to the spatial modulus $\mathbf{a}$. All other terms taking part in its assemblage in (35) are related to the geometry of finite deformations.

5.2. Explicit solution procedure

Physical considerations often require that the term expressing inertial effects be included in the equilibrium statement. For that purpose the original weak form (31) is modified by including the inertial force

$$\int_{\boldsymbol{\varphi}_{n+1}(\Omega)} \left(\frac{1}{J_{n+1}} \boldsymbol{\tau}_{n+1} : \nabla \boldsymbol{\eta} - \rho (\boldsymbol{b}_{n+1} - \boldsymbol{a}_{n+1}) \cdot \boldsymbol{\eta} \right) \mathrm{d}v - \int_{\boldsymbol{\varphi}_{n+1}(\partial \Omega_\sigma)} \boldsymbol{t}_{n+1} \cdot \boldsymbol{\eta} \, \mathrm{d}a = 0 \quad \forall \boldsymbol{\eta} \in \mathscr{V}, \tag{39}$$

where $\boldsymbol{a}_{n+1} := \ddot{\boldsymbol{d}}_{n+1}$ is the acceleration.

Unlike the implicit solution procedure, which is not restricted by requirements of stability, the explicit solution procedure is only conditionally stable with the permissible time step governed by the Courant stability limit (for detailed analysis see, for instance, [5,16]). However, small time steps, often below the stability limit, are enforced by the requirements of resolution of the short wave phenomena arising in

simulations of a wide range of practical problems, such as, for instance, damage induced by seismic events. A distinct advantage of explicit solution procedure is a fairly simple treatment of the frictional contact conditions which are often a main source of difficulty in the implicit based modelling of a number of practical applications governed by complex frictional contact conditions along the evolving interfaces. This, together with large costs associated with equation solution within the implicit procedure, are the main reasons behind frequent usage of explicit procedures in simulation of inherently quasi-static processes.

6. Adaptive solution update

For a large number of practically relevant solid mechanics problems involving large inelastic strains, the *optimal mesh configuration* changes continually throughout the deformation process. Often, due to element distortion, rapid solution degradation is experienced that precludes achievement of any solution for the region of large deformations of practical interest. Moreover, additional complexities emerge when material failure takes place and the numerical model has both to indicate the correct site of fracture onset and to efficiently re-mesh the critical zones. Therefore, the introduction of adaptive mesh refinement processes is crucial for the solution of large scale industrial problems, which necessitates (i) specification of an appropriate error estimation criterion, (ii) development of a strategy for adapting the mesh based on the error distribution (iii) automatic mesh generation tools, and (iv) appropriate transfer operators.

6.1. Error indicators

An elementary procedure for the error estimation may be defined by the replacement of the exact values of variables and relevant derivatives of the problem by some post-processed values obtained from the available finite element solution and the problem data. Such procedures have proved to be effective for linear problems, and their extension to elasto-plastic solids has been found to be an appropriate solution to the adaptive solution of a variety of strongly nonlinear solid mechanics problems [30,33].

However, for problems where the requirements of the physical problem necessitate a sharp resolution of high gradients of the state variables over a small region of the mesh, which, as a final outcome of the process, typically incorporates material failure along a line or a surface in two- or three-dimensional problems, respectively, an extension of the above error indicators has proved to be advantageous. In order to effectively model material failure the essential idea is to correlate the adaptive procedure to the underlying failure mechanism. Therefore, an error measure based on *rate of fracture indicators* is described in detail by Perić et al. [33], based on the principle that the adaptive procedure should not only capture the progression of the plastic deformation but also provide refined meshes at regions of possible material failure.

6.2. Transfer operations for evolving meshes

The history dependent nature of the process necessitates transfer of all relevant problem variables from the old mesh to the new one, as successive remeshing is applied during the process simulation. Hence, some suitable means for transferring the state variables between meshes, or *transfer operators*, needs to be defined [27,20,31,39,26].

After creating a new mesh, the transfer of displacement and history-dependent variables from the old mesh to a new one is required. Several important aspects of the transfer operation have to be addressed [27,20,31,39,26]: (i) consistency with the constitutive equations, (ii) requirement of equilibrium (which is fundamental for implicit FE simulation), (iii) compatibility of the history-dependent internal variables transfer with the displacement field on the new mesh, (iv) compatibility with evolving boundary conditions, (v) minimisation of the numerical diffusion of transferred state fields.

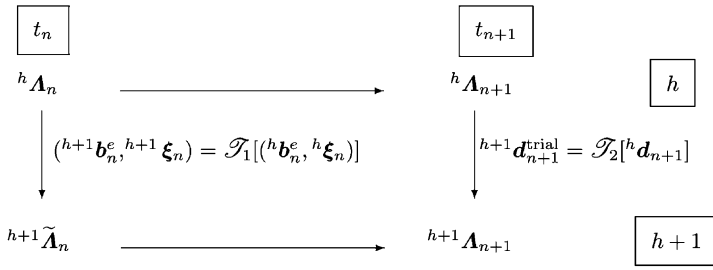

Fig. 2. Transfer operator diagram.

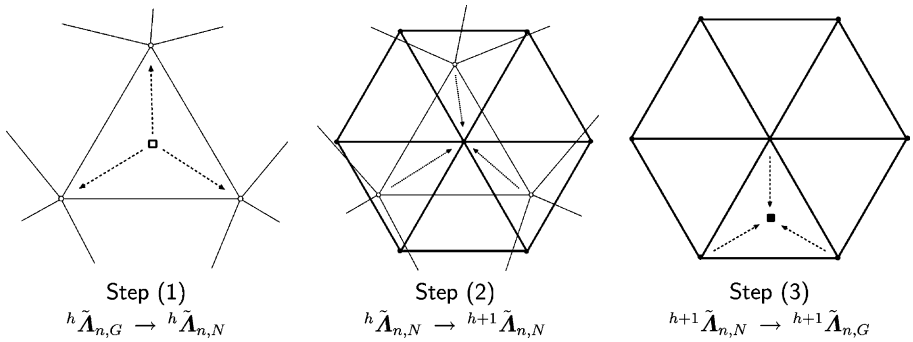

Fig. 3. A procedure illustrating the implementation of the transfer operator ${}^{h+1}\tilde{\boldsymbol{\Lambda}}_{n,G} = \mathscr{T}_1[{}^{h}\tilde{\boldsymbol{\Lambda}}_{n,G}]$ for finite element meshes composed of three noded triangles.

To briefly describe the transfer operation, let us define a state array ${}^{h}\boldsymbol{\Lambda}_n = ({}^{h}\boldsymbol{d}_n, {}^{h}\boldsymbol{F}_n, {}^{h}\boldsymbol{\tau}_n, {}^{h}\boldsymbol{b}^{e}_{n}, {}^{h}\boldsymbol{\xi}_n)$ where ${}^{h}\boldsymbol{d}_n, {}^{h}\boldsymbol{F}_n, {}^{h}\boldsymbol{\tau}_n, {}^{h}\boldsymbol{b}^{e}_{n}, {}^{h}\boldsymbol{\xi}_n$ denote values of the displacement, deformation gradient, stress tensor, the elastic left Cauchy–Green tensor, and a vector of internal variables at time t_n for the mesh h. Assume, furthermore, that the estimated error of the solution ${}^{h}\boldsymbol{\Lambda}_n$ respects the prescribed criteria, while these are violated by the solution ${}^{h}\boldsymbol{\Lambda}_{n+1}$. In this case a new mesh $h+1$ is generated and a new solution ${}^{h+1}\boldsymbol{\Lambda}_{n+1}$ needs to be computed. As the backward Euler scheme is adopted the internal variables ${}^{h+1}\boldsymbol{\xi}_n$ for a new mesh $h+1$ at time t_n need to be evaluated. In this way the state ${}^{h+1}\widetilde{\boldsymbol{\Lambda}}_n = (\cdot, \cdot, \cdot, {}^{h+1}\boldsymbol{b}^{e}_{n}, {}^{h+1}\boldsymbol{\xi}_n)$ is constructed, where a symbol $\widetilde{\ }$ is used to denote a reduced state array. It should be noted that this state characterises the history of the material and, in the case of a fully implicit scheme, provides sufficient information for computation of a new solution ${}^{h+1}\boldsymbol{\Lambda}_{n+1}$.

Conceptually, Fig. 2 summarises a typical transfer operation that includes both, the mapping of the internal variables and mapping of the displacement field. The implementation of the given general transfer operation is, for the case of evolving finite element meshes composed of constant strain triangles, illustrated in Fig. 3. Details of the above implementation procedure are provided in [31,33].

We point out that, for general unstructured and non-nested meshes, the transfer operation step almost invariably involves certain amount of numerical diffusion. For a recent analysis of currently employed transfer operation procedures in elasto-plasticity and evaluation of their accuracy we refer to [26].

7. Numerical examples

Numerical solutions of several problems from geological practice are provided in this section. They illustrate the scope and benefits of the Lagrangian finite element methodology in modelling a variety of problems associated with the salt tectonics.

In the first example simulation of a salt diapir formation is presented for a simple two layer system. The second and third examples provide numerical studies on finite element modelling of diapir formation during compression and folding and thin-skinned extension, respectively. The last example is a large scale simulation of diapirism in a basin due to progradation, which is typical for salt tectonics in the Gulf of Mexico.

All the simulations rely on extensive use of adaptive strategies described in Section 6, and serve to illustrate complex computational requirements imposed on solution of processes in the field of structural geology.

7.1. Diapir formation in a two layer system

In order to illustrate the capabilities of the Lagrangian approach in dealing with the Rayleigh–Taylor type instabilities and the formation of diapirs in the two material system, the simulation of a single salt diapir formation is performed. The problem geometry consists of a 2000 m thick viscoplastic overburden overlaying a 2500 m thick salt layer. The width of the model is 10,000 m and the boundary conditions consist of rollers on the side-walls and the base. In the initial state a sinusoidal perturbation is applied with an amplitude of 200 m. The density of the overburden is assumed to be $\rho_o = 3200$ kg/m^3 whilst the density of the salt is $\rho_s = 2200$ kg/m^3. An elasto-viscoplastic power law is used for both materials with properties based on Avery island rocksalt: fluidity $\gamma_0 = 0.176 \times 10^{-5}$ s^{-1}, yield stress $\sigma_Y = 9.15$ MPa, and the rate sensitivity exponent $N = 4$ (see [56] for further details on this choice of material properties).

A Lagrangian finite element methodology, and implicit solution strategy together with an adaptive re-meshing scheme is utilised. Fig. 4 shows the evolution of the material inversion with increasing time, while Fig. 5 gives the velocity field at a closing stage of a diapir formation.

This simple model problem illustrates the ability of the Lagrangian finite element description, in conjunction with adaptive re-meshing and an elasto-viscoplastic constitutive model, to represent complex material flows associated with salt diapirism. The model is based on an elasto-viscoplastic representation, unlike the previously published work, which generally treats all the material as a Newtonian fluid. This is an important point as it allow more accurate representation of the overburden, and its influence on salt deformations.

7.2. Shortening of a viscous source layer overlain by loose sand

Koyi [18] constructed a set of experiments to study the effect of pre-, syn- and post-diapiric shortening on moulding of diapirs. Each model consisted of a viscous layer of transparent silicone polymer gum (SGM36), to simulate the underlying salt, and overburdens of loose sand of differing thicknesses. The particular experiment considered consists of a 13 mm thick viscous layer buried under a 13 mm thick layer of loose sand which is shortened continuously at a rate of 18 mm/h (5×10^{-3} mm/s).

The model, shown in Fig. 6, is constructed using two material layers 13 mm thick and with a width of 130 mm (the width of the physical model is unknown). A geometric perturbation is used consisting of a 10% increase in the thickness of the salt layer at $\frac{1}{4}$ length. The layers are fully bonded and the base and vertical boundaries are prescribed using roller boundary conditions. The domain is shortened at a constant rate by an applied displacement at the right hand boundary. The constitutive properties for the silicone polymer gum and sand in the experiment were not clear. Approximate models are therefore constructed using an elasto-viscoplastic power law for the salt and an elastoplastic Mohr–Coulomb model for the loose sand. An adaptive re-meshing scheme is utilised in conjunction with a relatively coarse element discretisation with the target element size of 2 mm. A material grid, with 1 mm spacing, is superimposed on the original mesh to enable tracking of the evolution of the material flow.

In the physical model an anticline cored by the viscous material formed in the overburden. The forelimb of the fold overturned and ruptured as the shortening intensified pinching the core of the anticline and

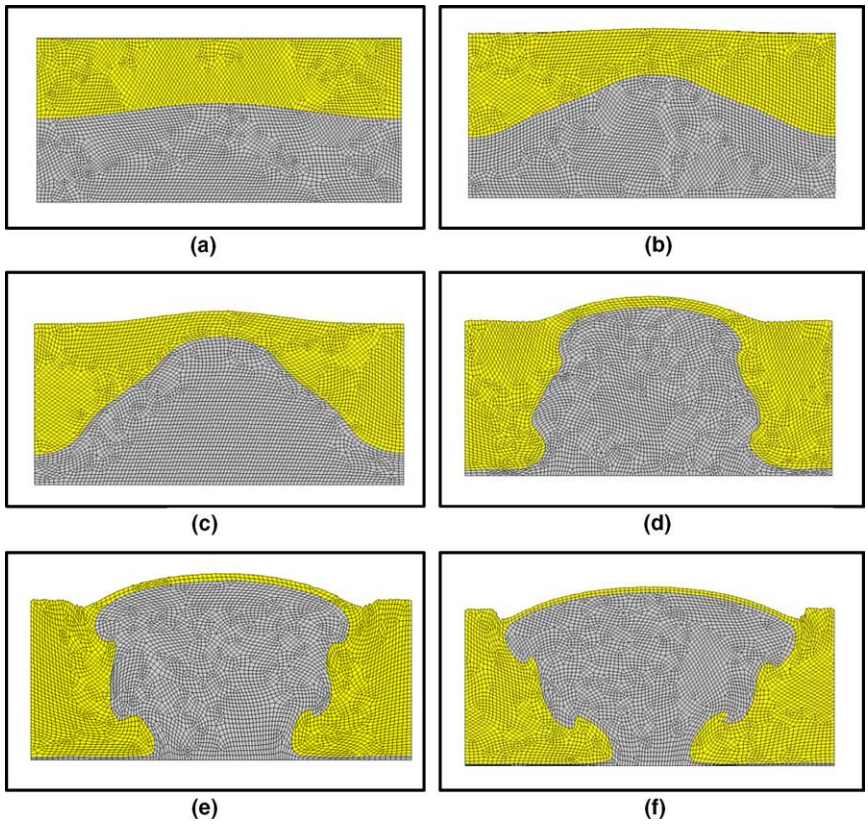

Fig. 4. Diapir formation in a two layer system: (a)–(f) evolution of finite element meshes during several stages of the diapir formation.

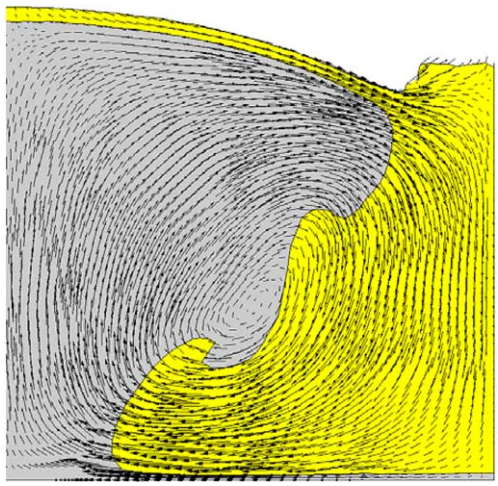

Fig. 5. Diapir formation in a two layer system: velocity field in a closing stage of the diapir formation.

Fig. 6. Shortening of a viscous layer overlain by loose sand: initial geometry and computational model.

separating it from the source layer. No diapirs could penetrate the overburden units that were tectonically thickened.

The behaviour of the computational model is in agreement with the physical experiment. Localisation of the deformation occurs in the sand at the location of the largest perturbation in the geometry (Fig. 7). This triggers the formation of an anticline that subsequently grows and contains a salt core (Fig. 8). Rupture of the fold was not included in the analysis but could be represented using a more sophisticated modelling strategy.

7.3. Simulation of diapirism in thin-skinned extension

Vendeville and Jackson [51] investigated thin-skinned extension, which is typical of the Gulf of Mexico, using physical two layer systems where the salt is represented by silicone and the overburden by dry quartz sand. The primary set of experiments were conducted in a 430×435 mm box at normal gravity using a 40 mm silicone sub-stratum, representing the salt, and a 55 mm overburden of well rounded, well sorted dry quartz sand to represent the overburden. The silicone was either SGM-36, with a density of 970 kg/m^3 or Silbione with a density of 1820 kg/m^3. The density of the overburden as 1760 kg/m^3 and the friction angle $\theta = 30$–$31°$. In the case of the diapir rise experiments, the rate of extension was generally 10 mm/h. Four experiments were performed and terminated at differing extensions to allow sections to be recovered.

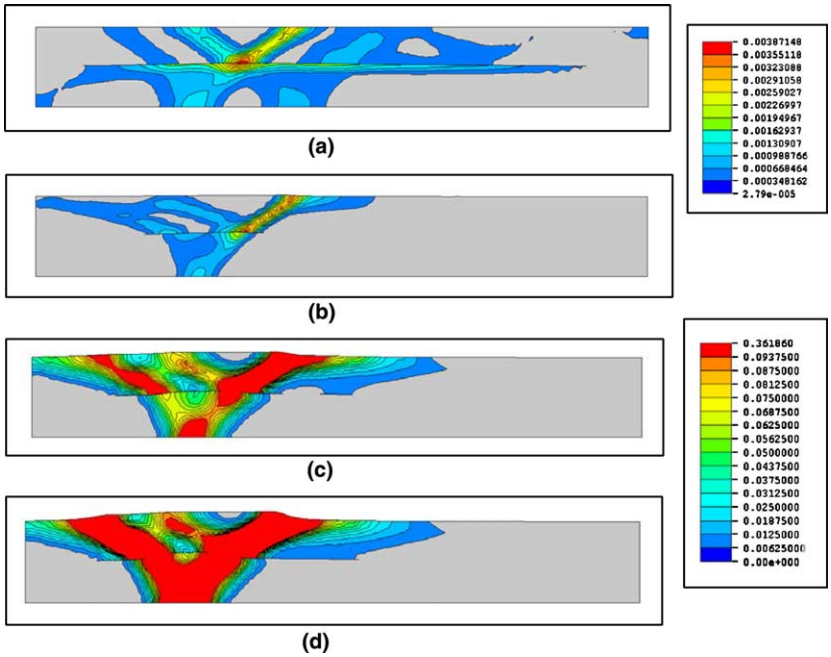

Fig. 7. Shortening of a viscous layer overlain by loose sand: (a) initial effective plastic strain distribution showing localisation of the loose sand; (b)–(d) evolution of effective plastic strain with progressive shortening.

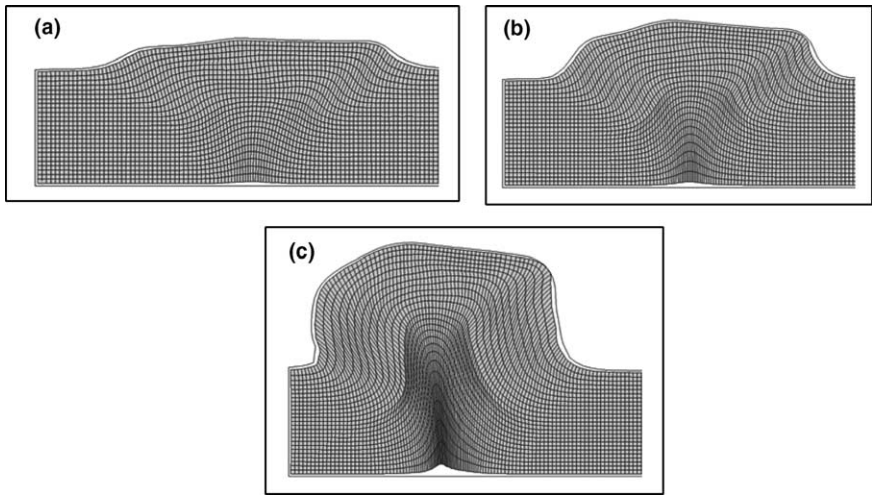

Fig. 8. Shortening of a viscous layer overlain by loose sand: (a)–(c) deformation of the material grid showing formation of anticline.

In the experiment a simple graben forms with two straight faults dipping towards each other (see Fig. 9). The graben indents the base layer and secondary faults are formed inside and parallel to one of the original boundary faults. The silicone upwells in the region where the overburden in thinnest. Further extension

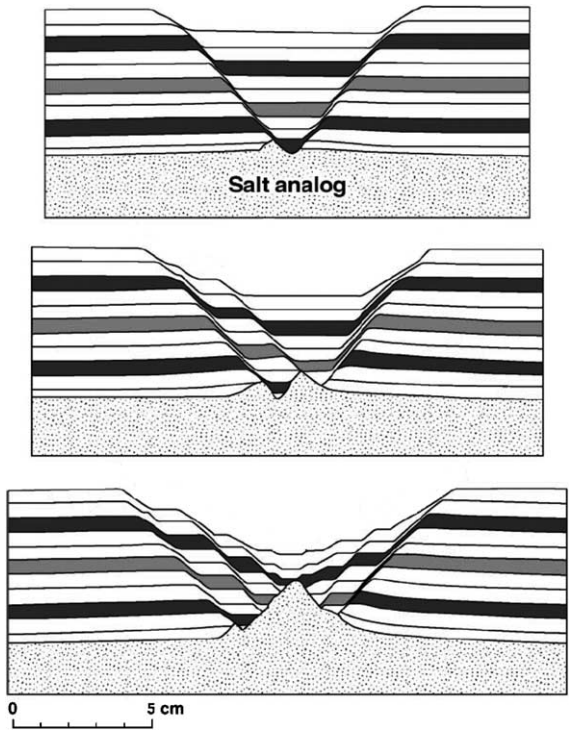

Fig. 9. Thin skinned extension: cross-section showing a reactive diapir underlying a graben [51]. Three experiments were performed under identical conditions but terminated at different times. The above cross-sections show the material state at the end of each test.

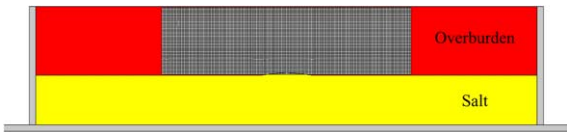

Fig. 10. Thin skinned extension: initial configuration.

results in the formation of further faults that slice the overburden in the faulted region into smaller blocks. Movement of these blocks permits a large, triangular diapir to approach the surface.

The computational model is constructed using two material layers inside a rigid box with movable side supports (Fig. 10). The lower layer of silicone representing the salt is 40 mm thick whilst the quartz sand upper overburden layer is 55 mm thick. The width of the box is taken as either 200 or 400 mm. The layers are fully bonded and the interface with the base and vertical boundaries are represented using a Mohr–Coulomb frictional interface law with a friction angle $v = 0.2$. The domain is lengthened by an applied displacement at both boundaries. A power law elasto-viscoplastic law is used for the silicone whilst an elastoplastic Mohr–Coulomb model is used for the quartz sand. Explicit solution strategy and an adaptive re-meshing scheme are utilised in conjunction with element discretisations with the target element size of between 1 and 2 mm. A material grid, with 1.25 mm spacing, is superimposed on the original mesh to enable tracking of the evolution of the material flow.

An initial perturbation is applied at the horizontal centre of the interface between the two layers to promote the formation of the initial damage at this location. However the symmetric failure exhibited by the experiment is difficult to reproduce numerically as:

- Accurate properties for the silicone are unknown.
- The load transfer from the viscous silicone layer to the brittle quartz layer can easily mobilise localised shear bands, equivalent to regional growth faults, which allow load shedding in the sand overburden prior to the formation of a graben.
- A half graben may initially form but prior to the formation of the second fault of the graben, shear bands equivalent to regional or counter regional growth faults form.

The results of two simulations are presented:

- *Case* 1 where a 400 mm long domain is used with lower wall friction (Figs. 11 and 12).
- *Case* 2 where a 300 mm long domain is used with higher wall friction (Figs. 13–15).

Note that the friction between the silicone and the box walls in case 2 is sufficiently high to prevent any slip on this boundary. This artificial boundary condition has a significant impact on the behaviour observed in the computational model. However the simulation provides several interesting insights into the interaction of the quartz sand and the silicone.

7.3.1. Case 1

At the location of the perturbation, low levels of damage lead to the activation of fault sloping right to left (Fig. 11). Movement on this fault promotes the activation of the second fault that forms a graben containing a clearly defined wedge of quartz sand that is lightly damaged. Continued extension results in further settlement of the graben surface accompanied by increasing damage of the material forming the wedge. The reduction in strength of the damaged material allied with the higher pressure in the silicone intrusion

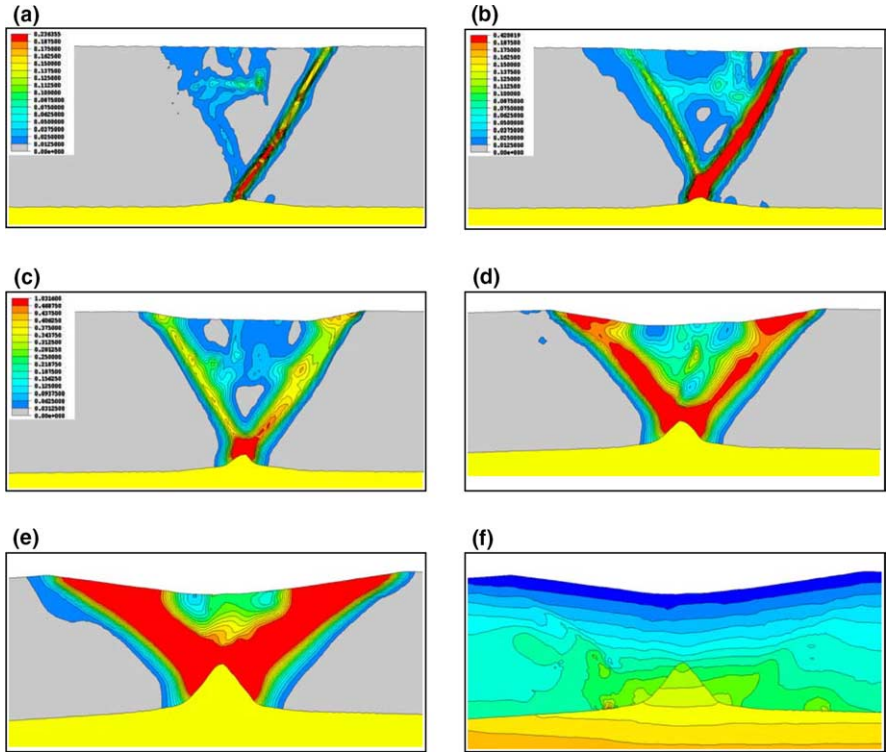

Fig. 11. Thin skinned extension: diapir formation in Case 1. (a)–(e) Equivalent plastic strain distribution at different stages of the diapir formation, (f) pressure distribution at a typical stage during reactive diapir intrusion.

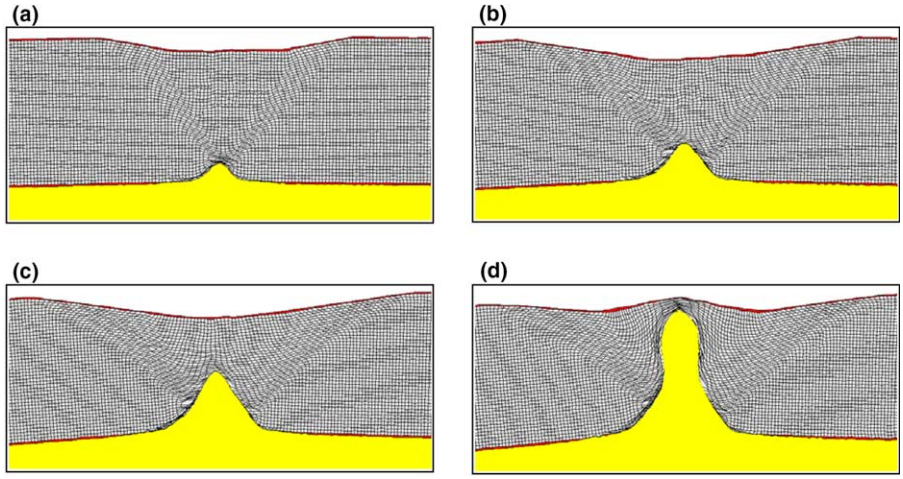

Fig. 12. Thin skinned extension: diapir formation in Case 1. (a)–(d) Material mesh evolution during several stages of diapir formation.

allows the diapir to gradually rise. This reactive behaviour is confirmed by the deformation of the material grid which exhibits no evidence of arching of the material above the diapir as it rises. Fig. 12(c) and (d)

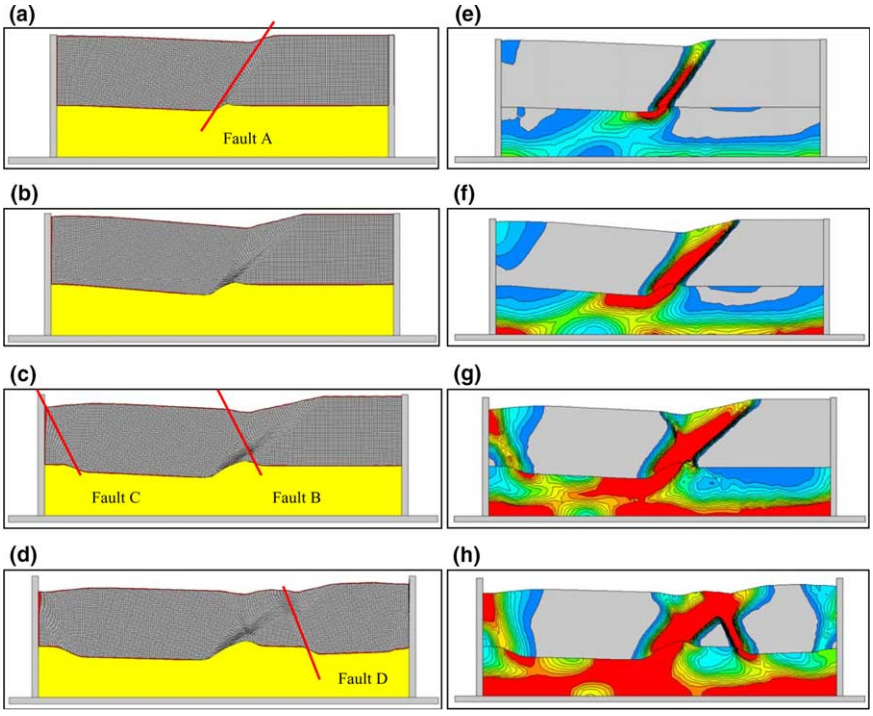

Fig. 13. Thin skinned extension: fault formation during the early phase of deformation for Case 2. (a)–(d) Material mesh, and (e)–(h) contours of equivalent plastic strain, during different stages of fault formation.

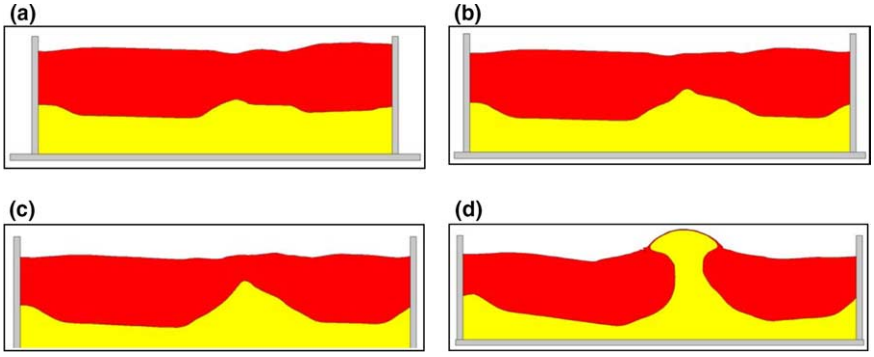

Fig. 14. Thin skinned extension: material plot showing stages of diapir formation in Case 2. (a) Early stage non-uniformity of interface, (b) reactive formation of diapir, (c) transition from reactive to active stage, (d) diapir after piercement.

show that the sand has been shouldered aside and the remaining overlying sand has been thinned by the quickly advancing silicone.

7.3.2. Case 2

The strong vertical constraint provided by the wall friction prevents a reduction in the thickness of the silicone layer at the wall boundaries (Figs. 13–15). Therefore when an initial fault forms (Fault A) at the centre of the domain (Fig. 13(a)), continued extension results in a movement on this fault together with

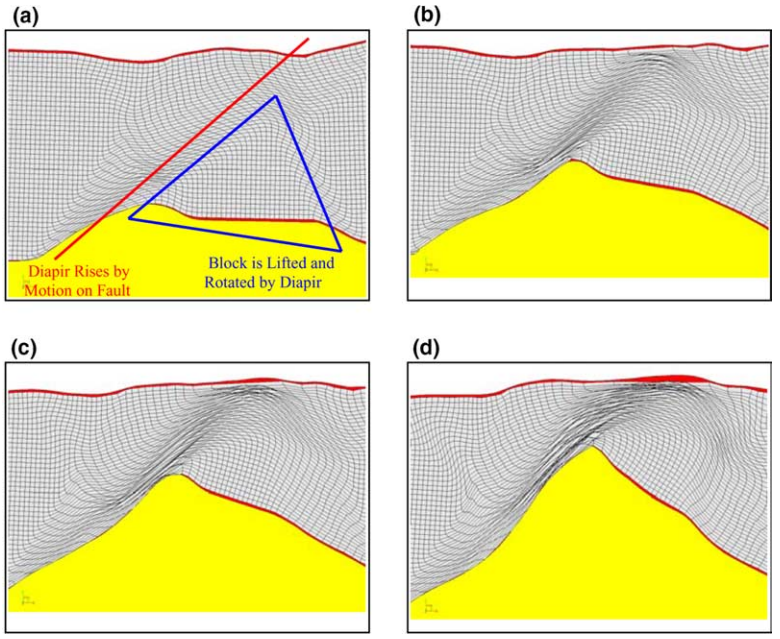

Fig. 15. Thin skinned extension: upwelling of diapir during transition from reactive to active stage in Case 2.

significant bending of the sand on the hanging wall of the fault. Secondary faulting (Faults B and C in Fig. 13(c)) at the wall boundary and at the centre of the domain forms a block of material that reduces in relief with further extension. A third regional growth fault (Fault D in Fig. 13(d)) then forms in the right hand block, allowing this block to reduce in relief with further extension.

As extension proceeds, the left and right hand blocks sink and the reduction of overburden due to the movement on fault D allows the salt to rise along the weakened line corresponding to Fault A (Fig. 14). The upwelling salt also uplifts/rotates and shoulders aside a wedge of intact overburden that lies between the fault lines (Fig. 15). This behaviour is characteristic of a diapir that evolves from reactive to active state. The diapir is initially reactive with the gain in relief of the diapir being governed by the kinematics of the overlying material. However, once the diapir pressure is sufficient to overcome the local strength of the material, active diapirism results in rapid piercement of the overburden.

7.3.3. Conclusions

The models have reproduced the key features ascribed by Vendeville and Jackson to reactive and active diapirs, namely:

- Initiation of rising diapirs as a result of movement of fault blocks created by regional extension.
- A clearly defined reactive stage where the diapir does not rise by forceful intrusion but via re-organization of the damaged overburden. Case 2 clearly shows the diapir growing by movement along the initial fault and that an overlying block is pushed aside as the diapir rises.
- An active stage where the diapir rapidly pierces the overburden by forceful intrusion of the underlying salt. The active intrusion of Case 1 shows the diapiric crest rises by lifting and thinning the overburden in the active stage. The characteristic rapid acceleration of the salt is exhibited in the simulations for both cases.
- A passive diapirism stage, i.e. Case 1 where the diapir spreads after piercing the overburden.

7.4. Prediction of salt-diapirism due to progradation

7.4.1. Overview

This is a model problem inspired by the centrifuged physical models of Gulf of Mexico profiles studied by Talbot [50]. In these experiments the crystalline basement beneath the northern Gulf of Mexico is represented using a $200 \times 70 \times 5$ mm layer of quasi-rigid plastilina. Irregularities in the prototype basement consist of a single ramp or step that simulates the Sigsbee uplift and limits the distal margin of the model salt. The Louann salt is represented by a rolled layer of plastic or viscous silicone putty that started with constant thickness in front of the distal basement step or ramp.

Progradation is achieved by adding, at normal gravity, approximately ten ductile loads that represent second order clinoforms deposited by 5–20 Ma of sedimentation. The clastic overburden was formed using a homogeneous mixture of powdered barium sulphate and silicone putty of differing densities. The material has a yield stress of a few hundred Pascal's and is characterized by a power law with exponent $N = 7$ at elevated gravity. The overburden is stiffer than the salt.

The box is spun in a large centrifuge to produce a gravity of $1000g$ for several minutes, which is deemed to be equivalent to 5–20 Ma of geological time. Five differing construction sequences are presented in the original research [50].

7.4.2. Description of the model

A computational model is constructed in a similar manner to the physical models presented by Talbot [50]. The aim of the model is to demonstrate the applicability of the computational model to this class of problem. Therefore in this feasibility study, the constructional sequence is simplified by reducing the number of load sequences. The key features of the model are:

- The model has similar dimensions to the physical model i.e. the width of the model is 200 mm with typical layer thicknesses of 5 mm.
- The base of the model is rigid and contains a step to simulate the Sigsbee uplift.
- Three layers of overburden are added sequentially. Each new layer is added 'body fitted' to the previously deformed layers.
- A $1000g$ gravity field was used during the relaxation phase for each layer.
- The constitutive properties of the salt and overburden are based on estimated properties for the physical model materials i.e. the initial yield stress for the salt and overburden are 515 and 615 Pa respectively, the viscosity of both layers is identical. The density of the salt is taken as 30% less than the density of the overburden. This differential is greater than in the physical model which amounted to 10–15%. An elasto-viscoplastic law described in Section 3.2.1 is used for all materials.
- A Coulomb friction law, with a coefficient of friction $v = 0.3$, represents the interaction between the layers.
- An explicit dynamic Lagrangian technique with automatic re-meshing is used.

7.4.3. Results

The construction sequence and the resulting deformation are illustrated in Fig. 16, whilst the re-orientation of the material is illustrated by the deformed material grid in Fig. 17. This feasibility study illustrates the key features of the gravity spreading exhibited by the physical models in the centrifuge i.e. early slope sinking maturing to gravity spreading that may be partitioned into two mechanisms:

- A zone at the crest of the slope dominated by vertical shortening and horizontal extensional shear that is uniform rather than localized to down to the basin faults. Lateral extensional shear suppresses the rise of buoyant diapirs so that no equivalents of salt rollers rise in the region of active extension.

- A zone of vertical thickening and horizontal shortening in the toe of the slope aided the rise of buoyant salt structures.

Other features of the predicted deformation, which match specific characteristics of the response observed by Talbot [50] in physical experiments, are:

- The zone of extensional shear fed material to the zone of shortening shear so that the two zones are genetically linked.

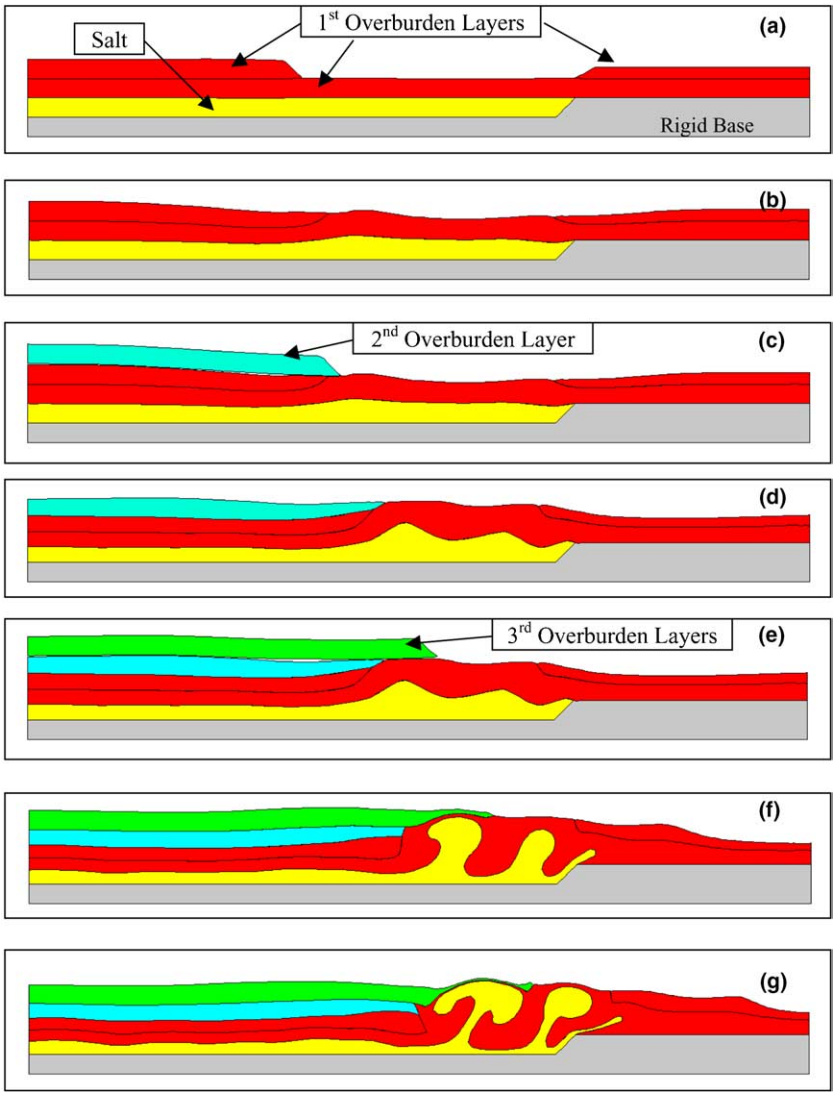

Fig. 16. Salt diapirism due to progradation. Evolution of material regions: (a) initial condition, (b) relaxation of first wedge, (c) application of second wedge, (d) relaxation of second wedge, (e) application of third wedge, (f) relaxation of third wedge showing fully formed diapers, (g) final configuration showing fully formed diapirs.

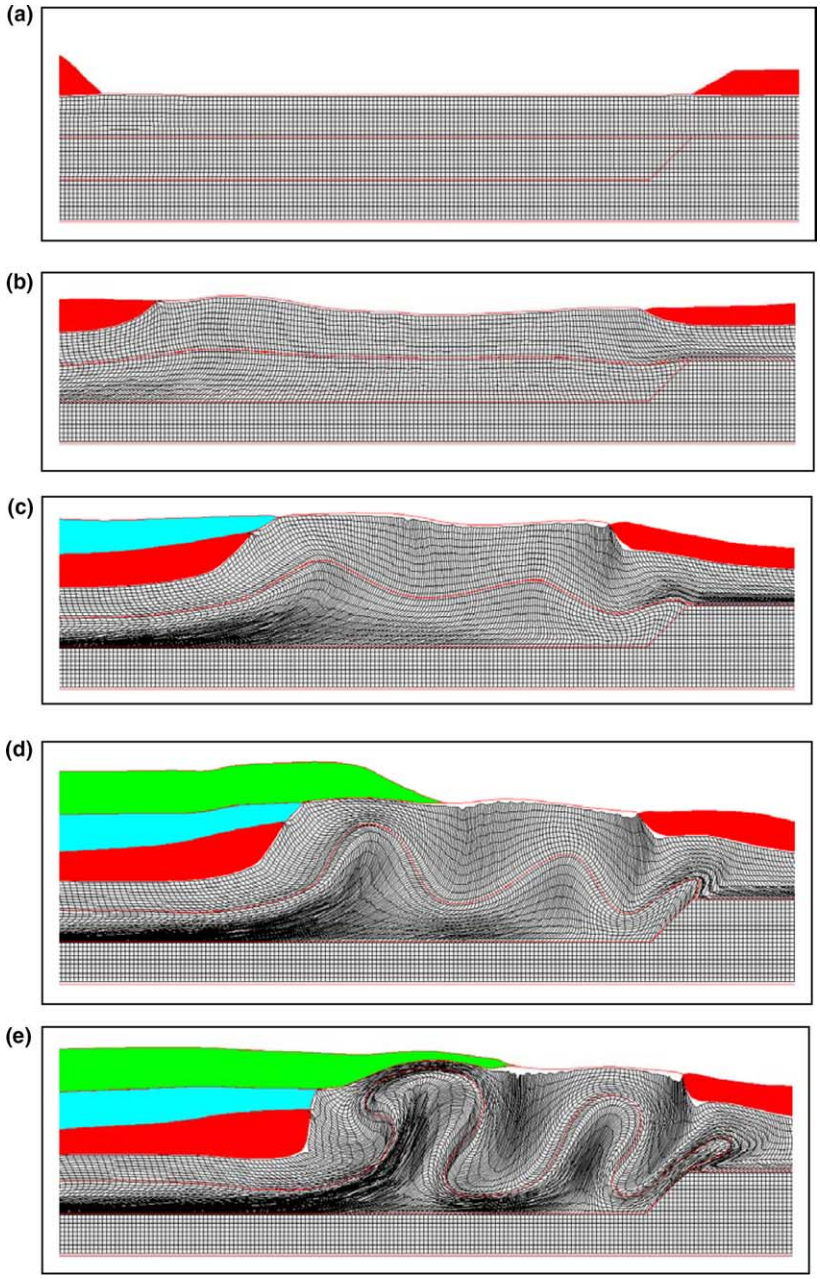

Fig. 17. Salt diapirism due to progradation. Evolution of the material deformation (deformation of the material grid identifies the material flow): (a) initial configuration, (b) relaxation of first wedge, (c) relaxation of second wedge, (d), (e) relaxation of third wedge.

- Horizontal shortening that followed early vertical shortening appears to have been far more significant than buoyancy in initiating most of the model structures. Most of the structures initiate as gentle buckles in the zone of lateral shortening. This is also the case in the computational model (Figs. 16 and 17).

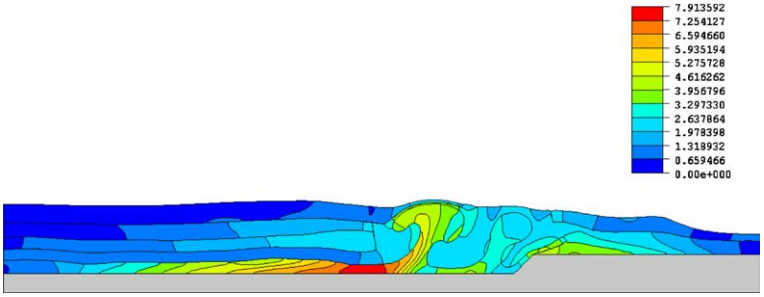

Fig. 18. Salt diapirism due to progradation. Distribution of effective plastic strain.

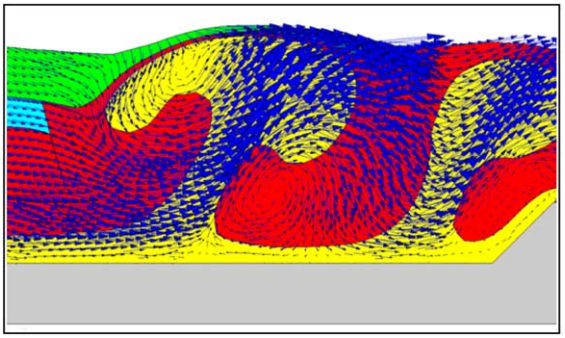

Fig. 19. Salt diapirism due to progradation. Vectors of velocity showing key areas of material movement.

- During the first two depositions, the salt is expelled basinwards and forms gentle bulges where the distal movement rates differ.

Examination of the distribution of effective plastic strain (Fig. 18) shows that the peak strains at this stage are of the order of 800%, whilst the velocity map (Fig. 19) clearly shows the impact of the rising diapirs in driving the deformation process.

7.4.4. Conclusion

This feasibility study is a preliminary application of a computational model to predicting the movement of salt due to long-term progradation of sediment. It clearly shows, however, that the methodology has the potential to provide significant benefits to understanding the mechanisms driving this important geological process.

8. Conclusion

Aspects of computational strategies for predictive geology are described in this paper, with particular reference to modelling of the salt tectonics.

A thermodynamically consistent framework has been presented for a unified description of inelastic solids incorporating combined elastic, elasto(visco)plastic and viscoelastic constitutive behaviours. It is argued that the presented approach offers efficient algorithmic framework for numerical analysis of a class of complex inelastic processes widely encountered in geological practice.

Some computational aspects of adaptive strategies for strongly nonlinear solid mechanics problems are briefly discussed and their use illustrated by means of numerical examples involving extremely large deformations of inelastic solids. It has been clearly demonstrated that an efficient and robust adaptive strategy is essential for successful simulation of large deformation problems encountered in the field of salt tectonics.

Numerical simulations have revealed the importance of the different mechanisms that may influence and promote the formation of salt diapirs. In particular, it has been demonstrated that the following mechanisms and conditions have important influence of on salt deformations and formation of diapirs: (i) compression and folding of overburden, (ii) thin-skinned extension, (iii) drag, (iv) differential loading due to progradation of sedimentation. Numerical results have also illustrated the importance of setting the appropriate boundary and initial conditions, and identifying realistic material parameters. Acknowledging difficulties and uncertainties related to evaluation of all necessary conditions and parameters, this clearly identifies the need for carefully designed experimental and numerical programme, and close collaboration of computational modellers with specialists in the field of structural geology.

Numerical simulations presented in the paper clearly illustrate the potential that Lagrangian finite element methodology offers to the field of predictive geology, which is concerned with analysis of geological structures and processes. In future studies, we are planning to focus on large scale three-dimensional simulation of salt tectonics on basin scale.

Acknowledgment

The support provided by E.C. Clukey of BP America Inc. is gratefully acknowledged. Partial support by the EPSRC of UK through Grant GR/R92318, awarded to the University of Wales Swansea, is also acknowledged.

References

[1] P. Bach, O. Hassager, An algorithm for the use of the Lagrangian specification in Newtonian fluid mechanics and applications to free-surface flow, J. Fluid Mech. 152 (1985) 173–190.
[2] K.J. Bathe, Finite Element Procedures, second ed., Prentice-Hall, Englewood Cliffs, NJ, 1996.
[3] T. Belytschko, W.K. Liu, B. Moran, Nonlinear Finite Elements for Continua and Structures, Wiley, New York, 2000.
[4] J.F. Besseling, E. van der Giessen, Mathematical Modelling of Inelastic Deformation, Chapman & Hall, London, 1994.
[5] T. Belytschko, An overview of semidiscretization and time integration procedures, in: T. Belytschko, T.J.R. Hughes (Eds.), Computational Methods for Transient Analysis, North-Holland, 1983, pp. 1–65.
[6] H. Berner, H. Ramberg, O. Stephansson, Diapirism in theory and experiment, Tectonophysics 15 (1972) 197–218.
[7] J.U. Brackbill, D.B. Kothe, C. Zemach, A continuum method for modelling surface tension, J. Comput. Phys. 100 (1992) 335–354.
[8] D.E. Carlson, A. Hoger, The derivative of a tensor-valued function of a tensor, Quart. Appl. Math. 44 (3) (1986) 409–423.
[9] M.A. Crisfield, Non-linear Finite Element Analysis of Solids and Structures. Volume 1: Essentials, John Wiley, Chichester, 1991.
[10] M.A. Crisfield, Non-linear Finite Element Analysis of Solids and Structures. Volume 2: Advanced Topics, John Wiley, Chichester, 1997.
[11] S. Chandrasekhar, Hydrodynamic and Hydromagnetic Stability, Oxford University Press, New York, 1961.
[12] N.D. Cristescu, U. Hunsche, Time Effects in Rock Mechanics, John Wiley, Chichester, 1998.
[13] A. Cuitiño, M. Ortiz, A material-independent method for extending stress update algorithms from small-strain plasticity to finite plasticity with multiplicative kinematics, Engrg. Comput. 9 (1992) 437–451.
[14] A. Eterovic, K.-J. Bathe, A hyperelastic based large strain elasto-plastic constitutive formulation with combined isotropic–kinematic hardening using the logarithmic stress and strain measures, Int. J. Numer. Methods Engrg. 30 (1990) 1099–1114.
[15] G.J. Frank, R.A. Brockman, A viscoelastic–viscoplastic constitutive model for glassy polymers, Int. J. Solids Struct. 38 (2001) 5149–5164.
[16] T.J.R. Hughes, The Finite Element Method. Linear Static and Dynamic Finite Element Analysis, Prentice-Hall, Englewood Cliffs, NJ, 1987.

[17] M.P.A. Jackson, C.J. Talbot, External shapes, strain rates and dynamics of salt structures, Geol. Soc. Am. Bull. 97 (1986) 305–323.
[18] H. Koyi, The shaping of salt diapirs, J. Struct. Geol. 20 (1998) 321–338.
[19] H. Koyi, C.J. Talbot, B.O. Torudbakken, Salt diapirs of the southwest Nordkapp Basin: analogue modelling, Tectonophysics 228 (1993) 167–187.
[20] N.-S. Lee, K.-J. Bathe, Error indicators and adaptive remeshing in large deformation finite element analysis, Fin. Elem. Anal. Design 16 (1994) 99–139.
[21] J. Lubliner, Plasticity Theory, Macmillan Publishing Company, New York, 1990.
[22] C. Miehe, Computation of isotropic tensor functions, Comm. Numer. Methods Engrg. 9 (1993) 889–896.
[23] C. Miehe, J. Keck, Superimposed finite elastic–viscoelastic–plastoelastic stress response with damage in filled rubbery polymers. Experiments, modelling and algorithmic implementation, J. Mech. Phys. Solids 48 (2000) 323–365.
[24] L.L. Nettleton, Fluid mechanics of salt domes, Am. Assoc. Pet. Geol. Bull. 18 (1934) 1175–1204.
[25] L.L. Nettleton, Recent experimental and geophysical evidence of mechanics of salt-dome formation, Am. Assoc. Pet. Geol. Bull. 27 (1943) 51–63.
[26] A. Orlando, D. Perić, Analysis of transfer procedures in elastoplasticity based on the error in constitutive equations: theory and numerical illustrations, Int. J. Numer. Methods Engrg. 60 (2004) 1595–1631.
[27] M. Ortiz, J. Quigley IV, Adaptive mesh refinement in strain localization problems, Comput. Methods Appl. Mech. Engrg. 90 (1991) 781–804.
[28] D. Perić, D.R.J. Owen, M. Honnor, A model for finite strain elasto-plasticity based on logarithmic strains: computational issues, Comput. Methods Appl. Mech. Engrg. 94 (1992) 35–61.
[29] D. Perić, On a class of constitutive equations in viscoplasticity: formulation and computational issues, Int. J. Numer. Methods Engrg. 36 (1993) 1365–1393.
[30] D. Perić, J. Yu, D.R.J. Owen, On error estimates and adaptivity in elastoplastic solids: application to the numerical simulation of strain localization in classical and Cosserat continua, Int. J. Numer. Methods Engrg. 37 (1994) 1351–1379.
[31] D. Perić, C. Hochard, M. Dutko, D.R.J. Owen, Transfer operators for evolving meshes in small strain elasto-plasticity, Comput. Methods Appl. Mech. Engrg. 137 (1996) 331–344.
[32] D. Perić, D.R.J. Owen, Finite element applications to the nonlinear mechanics of solids, Rep. Prog. Phys. 61 (1998) 1495–1574.
[33] D. Perić, M. Vaz Jr., D.R.J. Owen, On adaptive strategies for large deformations of elasto-plastic solids at finite strains: computational issues and industrial applications, Comput. Methods Appl. Mech. Engrg. 176 (1999) 279–312.
[34] D. Perić, E.A. de Souza Neto, A new computational model for Tresca plasticity at finite strains with an optimal parametrization in the principal space, Comput. Methods Appl. Mech. Engrg. 171 (1999) 463–489.
[35] D. Perić, W. Dettmer, A computational model for generalized inelastic materials combining elastic, viscoelastic and plastic material behaviour, Engrg. Comput. 20 (2003) 768–787.
[36] P. Perzyna, Fundamental problems in viscoplasticity, Adv. Appl. Mech. 9 (1966) 243–377.
[37] R. Radovitzky, M. Ortiz, Lagrangian finite element analysis of Newtonian fluid flows, Int. J. Numer. Methods Engrg. 43 (1998) 607–619.
[38] H. Ramberg, Gravity, Deformation and the Earth's Crust in Theory, Experiments and Geological Application, Academic Press, London, 1981.
[39] M.M. Rashid, Material state remapping in computational solid mechanics, Int. J. Numer. Methods Engrg. 55 (2002) 431–450.
[40] S. Reese, S. Govindjee, A theory of finite viscoelasticity and numerical aspects, Int. J. Solids Struct. 35 (1998) 3455–3482.
[41] J.A. Sethian, Level Set Methods and Fast Marching Methods, Cambridge University Press, 1999.
[42] W. Shyy, H.S. Udaykumar, M.M. Rao, R.W. Smith, Computational Fluid Dynamics with Moving Boundaries, Taylor & Francis, 1996.
[43] J.C. Simo, On a fully three-dimensional finite-strain viscoelastic damage model: formulation and computational aspects, Comput. Methods Appl. Mech. Engrg. 60 (1987) 153–173.
[44] J.C. Simo, Algorithms for static and dynamic multiplicative plasticity that preserve the classical return mapping schemes of the infinitesimal theory, Comput. Methods Appl. Mech. Engrg. 99 (1992) 61–112.
[45] J.C. Simo, C. Miehe, Associative coupled thermoplasticity at finite strains: formulation, numerical analysis and implementation, Comput. Methods Appl. Mech. Engrg. 98 (1992) 41–104.
[46] J.C. Simo, T.J.R. Hughes, Computational Inelasticity, Springer Verlag, New York, 1998.
[47] E.A. de Souza Neto, D. Perić, A computational framework for a class of fully coupled models for elastoplastic damage at finite strains with reference to the linearization aspects, Comput. Methods Appl. Mech. Engrg. 130 (1996) 179–193.
[48] S. Stewart, M. Coward, Synthesis of salt tectonics in the southern North Sea, Marine Petr. Geol. 12 (1995) 457–475.
[49] C.J. Talbot, Inclined and asymmetric upward-moving gravity structures, Tectonophysics 42 (1977) 159–181.
[50] C.J. Talbot, Centrifuged models of Gulf of Mexico profiles, Marine Petr. Geol. 9 (1992) 412–432.
[51] B.C. Vendeville, M.P.A. Jackson, The rise of diapirs during thin-skinned extension, Marine Petr. Geol. 9 (1992) 331–353.
[52] D. Waltham, Why does salt start to move?, Tectonophysics 282 (1997) 117–128.

[53] G. Weber, L. Anand, Finite deformation constitutive equations and a time integration procedure for isotropic, hyperelastic–viscoplastic solids, Comput. Methods Appl. Mech. Engrg. 79 (1990) 173–202.
[54] W.-D. Woidt, Finite element calculations applied to salt dome analysis, Tectonophysics 50 (1978) 369–386.
[55] S. Zaleski, P. Julien, Numerical simulation of Rayleigh–Taylor instability for single and multiple salt diapirs, Tectonophysics 206 (1992) 55–69.
[56] O.M.L. Yahya, M. Aubertin, M.R. Julien, A unified representation of the plasticity, creep and relaxation behavior of rocksalt, Int. J. Rock. Mech. Mining Sci. 37 (2000) 787–800.
[57] O.C. Zienkiewicz, R.L. Taylor, The Finite Element Method—Vol. 2: Solid Mechanics, Butterworth-Heinemann, 2000.